

Molecular-Level Understanding of Continuous Growth from Iron-Oxo Clusters to Iron Oxide Nanoparticles

Hogeun Chang,^{†,‡,▽} Byung Hyo Kim,^{†,‡,▽} Hu Young Jeong,[§] Jeong Hee Moon,[⊥] Minwoo Park,^{||} Kwangsoo Shin,^{†,‡,||} Sue In Chae,^{†,‡} Jisoo Lee,^{†,‡} Taegyung Kang,^{†,‡} Back Kyu Choi,^{†,‡} Jiwoong Yang,^{†,‡,||} Megalamane S. Bootharaju,^{†,‡} Hyoin Song,^{†,‡} Seong Hee An,[#] Kyung Man Park,[#] Joo Yeon Oh,^{||} Hoonkyung Lee,^{||} Myung Soo Kim,^{*,†,‡} Jungwon Park,^{*,†,‡,||} and Taeghwan Hyeon^{*,†,‡,||}

[†]Center for Nanoparticle Research, Institute for Basic Science (IBS), Seoul 08826, Republic of Korea

[‡]School of Chemical and Biological Engineering, and Institute of Chemical Process, Seoul National University, Seoul 08826, Republic of Korea

[§]UNIST Central Research Facilities (UCRF), Ulsan National Institute of Science and Technology (UNIST), Ulsan 44919, Republic of Korea

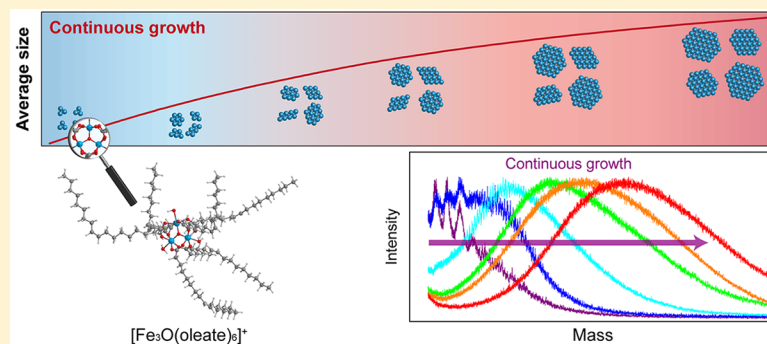
[⊥]Disease Target Structure Research Center, Korea Research Institute of Bioscience and Biotechnology (KRIBB), Daejeon 34141, Republic of Korea

^{||}Department of Physics, Konkuk University, Seoul 05029, Republic of Korea

[#]Department of Chemistry, Seoul National University, Seoul 08826, Republic of Korea

^{||}ASTA, Suwon 07675, Republic of Korea

Supporting Information



ABSTRACT: The formation of inorganic nanoparticles has been understood based on the classical crystallization theory described by a burst of nucleation, where surface energy is known to play a critical role, and a diffusion-controlled growth process. However, this nucleation and growth model may not be universally applicable to the entire nanoparticle systems because different precursors and surface ligands are used during their synthesis. Their intrinsic chemical reactivity can lead to a formation pathway that deviates from a classical nucleation and growth model. The formation of metal oxide nanoparticles is one such case because of several distinct chemical aspects during their synthesis. Typical carboxylate surface ligands, which are often employed in the synthesis of oxide nanoparticles, tend to continuously remain on the surface of the nanoparticles throughout the growth process. They can also act as an oxygen source during the growth of metal oxide nanoparticles. Carboxylates are prone to chemical reactions with different chemical species in the synthesis such as alcohol or amine. Such reactions can frequently leave reactive hydroxyl groups on the surface. Herein, we track the entire growth process of iron oxide nanoparticles synthesized from conventional iron precursors, iron-oleate complexes, with strongly chelating carboxylate moieties. Mass spectrometry studies reveal that the iron-oleate precursor is a cluster comprising a tri-iron-oxo core and carboxylate ligands rather than a mononuclear complex. A combinatorial analysis shows that the entire growth, regulated by organic reactions of chelating ligands, is continuous without a discrete nucleation step.

INTRODUCTION

The formation mechanism of inorganic colloidal nanoparticles has been generally understood by classical colloid chemistry based on nucleation and growth processes. The thermodynamic aspects of nucleation—the generation of small solid-

phase crystals from the assembly of minimal binding units (monomers)^{1–3}—are important for regulating the entire

Received: February 13, 2019

Published: April 9, 2019

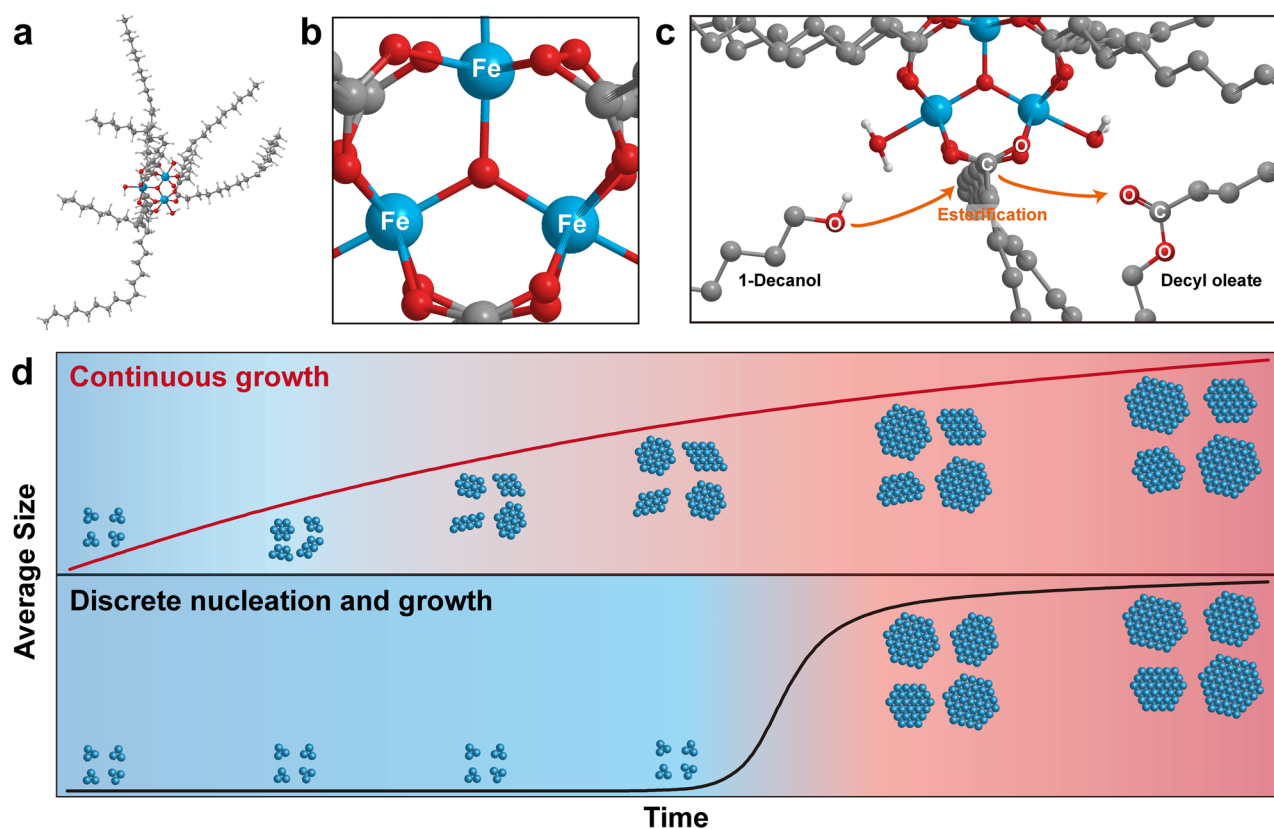


Figure 1. Structure of iron-oleate complex and continuous growth of iron-oxo clusters. (a) Computed trinuclear-oxo carboxylate structure of iron-oleate complex ($[\text{Fe}_3\text{O}(\text{C}_{18}\text{H}_{33}\text{O}_2)_6]^+$). (b) Core structure of iron-oleate complex. (c) Proposed reaction mechanism of continuous growth induced by esterification. (d) Schematic of continuous growth proposed in this paper and that of discrete nucleation and growth. Compared to discrete nucleation and growth, continuous growth does not show a distinct nucleation step but shows gradual growth.

nanoparticle formation process. The free energy of nuclei can be estimated as the sum of surface and bulk free energies.³ Owing to the strong dependency of surface energy on size, a critical size exists below which dissolution of thermodynamically unstable particulates occurs. To overcome the thermodynamic energy barrier to nucleation, the monomer concentration needs to exceed the supersaturation level, whereby a significant number of monomers form stable nuclei. During the homogeneous nucleation process to synthesize nanoparticles, supersaturation of monomers can be induced by various methods including rapid injection of precursors into a hot surfactant solution, gradual “heat-up” of the reaction mixture, and conversion of the precursors into monomers with reduced solubility.^{4–9} Recent studies reveal that monomers with different chemical states, such as small molecular species and clusters containing a few metal atoms or ions,^{10–14} participate in the formation of colloidal nanoparticles. In the subsequent growth regime, nuclei grow into nanoparticles via monomer attachment or coalescence events between the particles.^{12,15–17} The surface energy of the growing nanoparticles controls not only the growth rate but also their resulting sizes and morphologies.¹⁸

Various experimental approaches have been employed to understand the formation mechanisms of nanoparticles.^{5,6,19–27} These are mostly focused on semiconductor nanoparticles as can be easily tracked with their size-specific optical properties. The formation of the nanoparticles is generally controlled by dynamic fluctuations between the growing nanoparticles and surface ligands, which bind to both

molecular precursors and monomers.^{6,28–31} The strength of the binding moieties affects important stages during the growth of nanoparticles. For example, weakly binding moieties, such as CdSe–amine bonding, are susceptible to fast decomposition of the molecular precursors to generate a burst of nuclei.^{28–31} In the opposite case, in the presence of strongly binding moieties, such as CdSe–phosphonate bonding, the rate of nucleation is reduced by delaying the precursor decomposition.⁶ In addition, the reactivity of the chalcogenide source and the reaction temperature concurrently influence the regulation of the growth rate. Important roles of intermediates during the growth from precursors to nanoparticles have also been observed in several systems of metal chalcogenide nanoparticles.^{32–34}

The formation mechanism of metal oxide nanoparticles can be inherently different from that of metal chalcogenides due to several unique chemical aspects of their synthesis process. During a typical synthesis of metal oxide nanoparticles, molecular precursors include metal carboxylate moieties and the carboxylate group stays on the surface of the nanoparticles throughout the process. The carboxylate binding moieties include oxygen atoms and normally act as an oxygen source during the formation of the metal oxide nanoparticles. Based on the hard/soft acid–base theory, carboxylates are a hard base. As a result, they can strongly coordinate hard metal ions, such as Fe^{3+} , on the surface of the metal oxide nanoparticles.³⁵ When the carboxylate ligands on the surface of precursors or nanoparticles are eliminated by thermal decomposition or chemical reaction, the reactive hydroxyl groups or radicals are

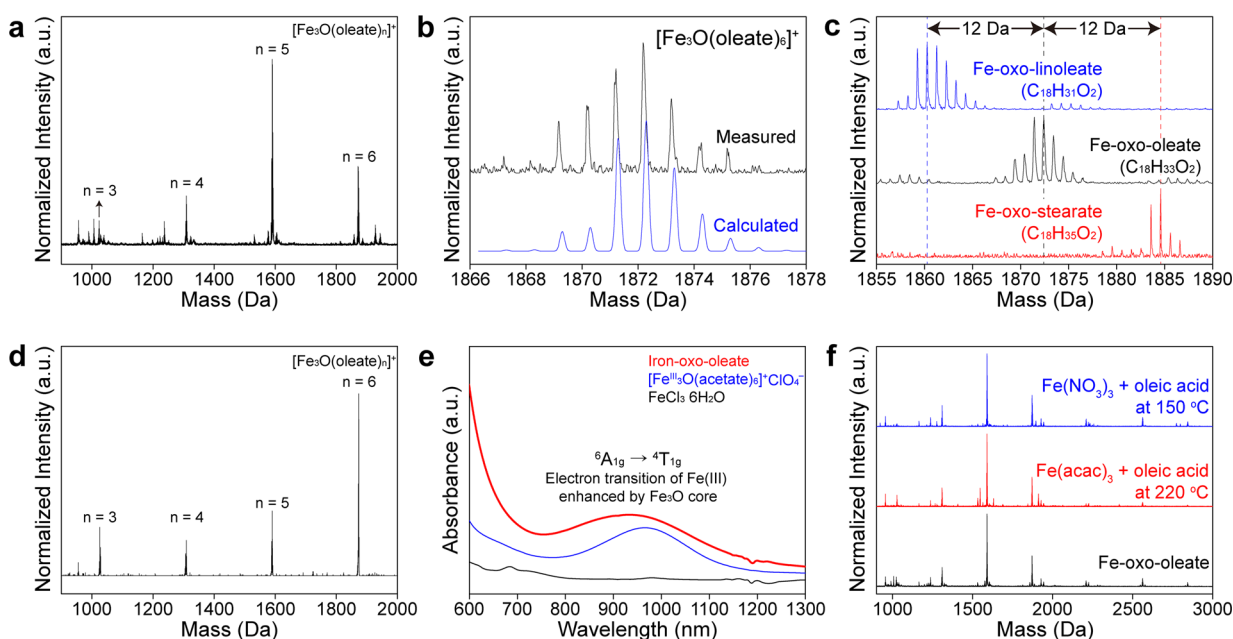


Figure 2. Characterization of iron-oxo-oleate complex. (a) MALDI-TOF mass spectra of iron-oxo-oleate complex. Main peaks of iron-oxo-oleate are assigned in the mass spectra. (b) Isotope calculation of the main peak at $m/z = 1872$. (c) MALDI-TOF mass spectra of iron-oxo carboxylates having different numbers of double bonds in the ligand. (d) TOF-TOF mass spectrum of $[\text{Fe}_3\text{O}(\text{oleate})_6]^+$ ($m/z = 1872$). (e) Near-infrared absorption spectra of iron complexes. Absorption wavelength and extinction molar coefficient are presented in Table S1. (f) Emergence of iron-oxo-oleate complex in mass spectra starting from different iron salts.

temporarily retained on the metal ions. Chemical reactions between them can induce direct interactions between nanoparticles and frequently promote the growth of metal oxide nanoparticles.^{5,36–39} Such unique thermodynamic characteristics of carboxylate moieties and their mechanistic behaviors imply that they may strongly control the formation of metal oxide nanoparticles from the initial transition of molecular precursors to small particulates and to the growth into large nanoparticles. In this case, the size of the particles in the range below the critical nucleus size, where intermediate species are thermodynamically unstable, typically observed in the formation of other types of nanoparticles, can become narrow or even absent.

Herein, we used various characterization methods including matrix-assisted laser desorption/ionization time-of-flight mass spectrometry (MALDI-TOF MS), nuclear magnetic resonance (NMR) spectroscopy, transmission electron microscopy (TEM), and *in situ* X-ray scattering to study the entire formation process of iron oxide nanoparticles. We confirmed that iron-oleate complexes, the representative precursors of iron oxide nanoparticles,⁴⁰ have a cluster structure containing a tri-iron-oxo carboxylate (Figure 1a,b). More importantly, we reveal that the entire process is continuous without any discrete nucleation event (Figure 1c,d), whereas the growth from tri-iron-oxo clusters to larger-sized iron-oxo clusters and eventually to iron oxide nanoparticles is driven by esterification of ligand moieties. Our findings provide new insights regarding the importance of ligand binding moieties and their reactions in metal oxide nanoparticle formation.

RESULTS AND DISCUSSION

Characterization of Iron-Oleate Complexes. We study the complete growth process of the formation of iron oxide nanoparticles from iron-oleate precursors. The oleate ligands strongly bind to the metal center of the precursors and

passivate the surface of the growing nanoparticles. As the energetics of precursors determines the chemical transformation in the early stage, identification of the precursor structure is a prerequisite for understanding the initiation of the reaction. We first characterized the iron-oleate complex by MALDI-TOF MS, Fourier transform infrared (FT-IR), and near-infrared spectroscopies.

MALDI-TOF MS is a powerful tool to characterize the exact molecular weight of metal–ligand complexes with minimal molecular fragmentation. The mass spectrum of the iron-oleate complex, which was synthesized from the reaction of iron chloride hexahydrate and sodium oleate, shows two main peaks ($m/z = 1872$ and 1591) in the high-mass region, as shown in Figure 2a. Isotope calculation of the main peak at $m/z = 1872$ confirms that the chemical structure of the iron-oleate complex is $[\text{Fe}_3\text{O}(\text{C}_{17}\text{H}_{33}\text{COO})_6]^+$, which we refer to as a tri-iron-oxo carboxylate complex (Figure 2b). The six coordinating oleate groups are further verified by comparing the molecular weight of the iron-oleate ($m/z = 1872$) with those of iron-stearate ($m/z = 1884$) and iron-linoleate ($m/z = 1860$) complexes, which show differences of $+12$ and -12 Da, respectively. Given that stearate (MW = 283.27 Da), oleate (MW = 281.25 Da), and linoleate (MW = 279.23 Da) have similar structures with a molecular weight difference of 2 Da of the two hydrogen atoms consecutively, the measured difference of 12 Da indicates that all the complexes contain six ligands (Figure 2c). Another main peak at $m/z = 1591$, with a difference corresponding to the mass of oleate ions, originates from the fragments of the iron-oleate complex during the measurement. TOF-TOF analysis further supports that the parent iron-oleate peak ($m/z = 1872$) can be broken into another main peak ($m/z = 1591$) (Figure 2d). It is noteworthy that a coordinated structure with six long-chain carboxylates are consistently observed regardless of the chemical structures of the ligands.

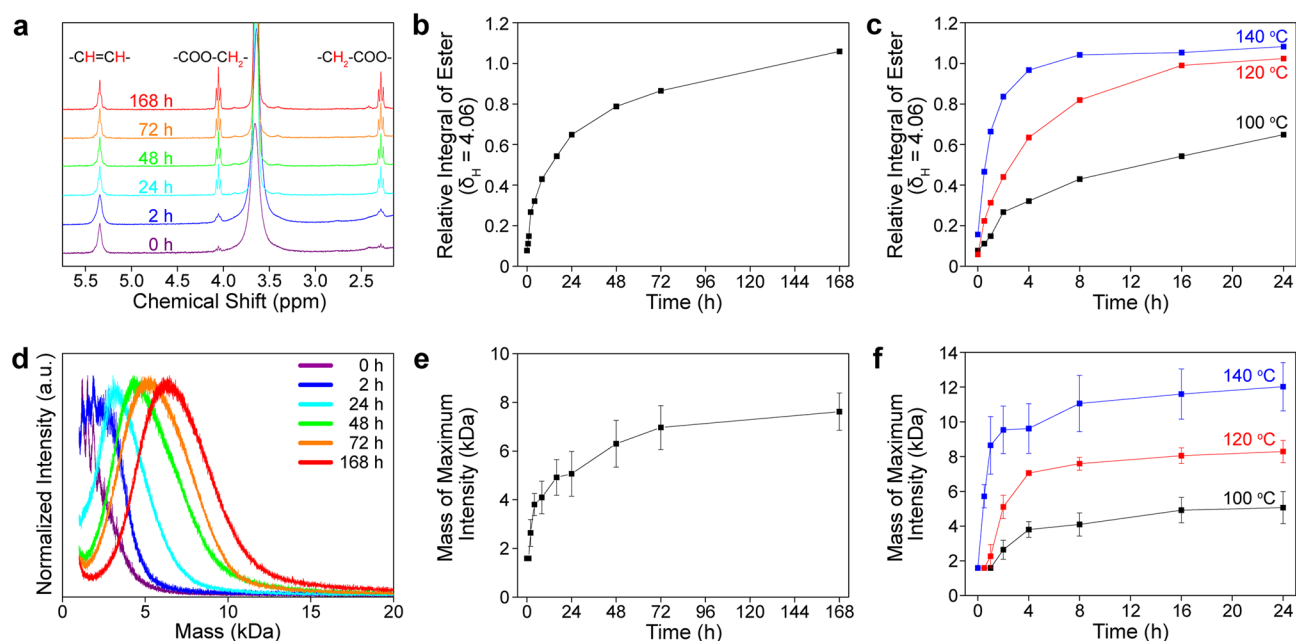


Figure 3. Evidence of continuous growth from the precursor to iron-oxo cluster at 100, 120, and 140 °C. (a) Change in ^1H NMR acquired from *ex situ* samples at 100 °C for 7 days. Strong peak observed at 3.6 ppm is assigned to hydroxyl hydrogen of 1-decanol. (b) Change in relative integral of ester at 100 °C for 7 days. (c) Change in relative integral of ester at different temperatures for 1 day. (d) Change in mass spectra at 100 °C for 7 days. (e) Change in mass of maximum intensity at 100 °C for 7 days. (f) Change in mass of maximum intensity at different temperatures for 1 day. Average and standard error of the mass of maximum intensity are presented in (e,f).

The presence of a tri-iron-oxygen center in the iron-oleate complex is supported by various spectroscopic measurements, which have been commonly used to characterize various metal carboxylates containing metal-oxo centers.^{41–47} The triangular structure strongly absorbs near-infrared light at 935 nm (Figure 2e). This absorption band is assigned to the $^6\text{A}_{1g}$ to $^4\text{T}_{1g}$ electron transition in the pseudo-octahedral Fe^{3+} ion.^{44,45} A similar structure having a shorter carboxylate chain presents a comparable absorbance at 965 nm. On the contrary, iron chloride, which does not contain a metal oxygen center, barely absorbs near-infrared light (800–1300 nm). The vibrational mode of Fe_3O is observed at approximately 600 cm^{-1} in the IR spectrum (Figure S1). The wavenumber for this absorption is consistent with the previous report on trinuclear-oxo carboxylate complexes.⁴⁶ The binding nature of carboxylate ligands within the complex can be verified by comparing the wavenumber difference between the symmetric and asymmetric vibrations of the carboxyl group.⁴⁸ The wavenumber difference of 160 cm^{-1} indicates that the oleate ligand is bound to iron in the bridging mode. In the structure of the iron-oleate complex, three iron ions are bound to the central μ_3 -oxygen, and six carboxylates bridge the iron ions, as illustrated in Figure 1a,b. The tri-iron-oxo carboxylate complex, $[\text{Fe}_3\text{O}(\text{RCOO})_6]^+$, has been reported as a stable triangular structure.^{27,42–45} Overall chemical composition of iron-oxo-oleate is proposed as $[\text{Fe}_3\text{O}(\text{C}_{18}\text{H}_{33}\text{O}_2)_6]^+(\text{C}_{18}\text{H}_{33}\text{O}_2)^-(\text{C}_{18}\text{H}_{33}\text{O}_2\text{H})_2(\text{H}_2\text{O})_3$ based on elemental analysis (Table S2).

Consistent occurrence of iron-oxo-oleate is also observed during the formation of iron oxide nanoparticles from different iron precursors including iron chloride (FeCl_3), iron acetylacetonate ($\text{Fe}(\text{acac})_3$), and iron nitrate ($\text{Fe}(\text{NO}_3)_3$). When high enough temperature is applied to activate the precursor salts to be decomposed, the peak patterns from the two different mixtures ($\text{Fe}(\text{acac})_3$ + oleic acid and $\text{Fe}(\text{NO}_3)_3$ + oleic acid), shown in Figure 2f, are nearly identical to that of

iron-oleate complex synthesized using FeCl_3 . The common appearance of trinuclear-oxo-oleate in several synthetic pathways confirms the structural stability and similarity of the events at the early stage of the synthesis. We could elucidate the structure of iron-oleate precursors, which are generally used for the synthesis of iron oxide nanoparticles. Our findings demonstrate that the iron-oleate precursor is not a complex containing a single metal atom center but a cluster with three iron ions bound to μ_3 -oxygen.

Continuous Growth Mechanism of Iron Oxide Nanoparticles. We studied the formation process of iron oxide nanoparticles from the iron-oxo-oleate complexes by using NMR spectroscopy, MALDI-TOF MS, and aberration-corrected TEM. Briefly, the reaction rate is controlled to be slow by keeping the temperature below 200 °C to allow a time-series analysis of the ongoing reaction and avoid complications that might occur at high temperatures (Figure S6).⁴⁹ 1-Decanol is used for multiple purposes including as a solvent and a reaction promoter.³⁵

When the iron-oxo-oleate complex is reacted with an excess amount of 1-decanol at 100 °C, the solution gradually turned dark brown from reddish-brown. The products of this reaction are tracked by NMR spectra to investigate the reaction mechanism. Two strong peaks ($\delta_{\text{H}} = 4.06, 2.29$) that correspond to the ester group are observed in the NMR spectra (Figure 3a). The ester peaks presumably originate from decyl oleate, which is produced from the esterification of 1-decanol and the oleate group in the iron-oxo-oleate complex. The presence of decyl oleate from the beginning of the reaction indicates that the formation of nanoparticles is initiated by the esterification reaction of the ligands strongly binding to the tri-iron μ_3 -oxygen core. NMR and LC-MS analyses of the byproducts from the reaction mixture also confirm that decyl oleate is produced from the esterification reaction (Figures S7 and S8). The extent of reaction is

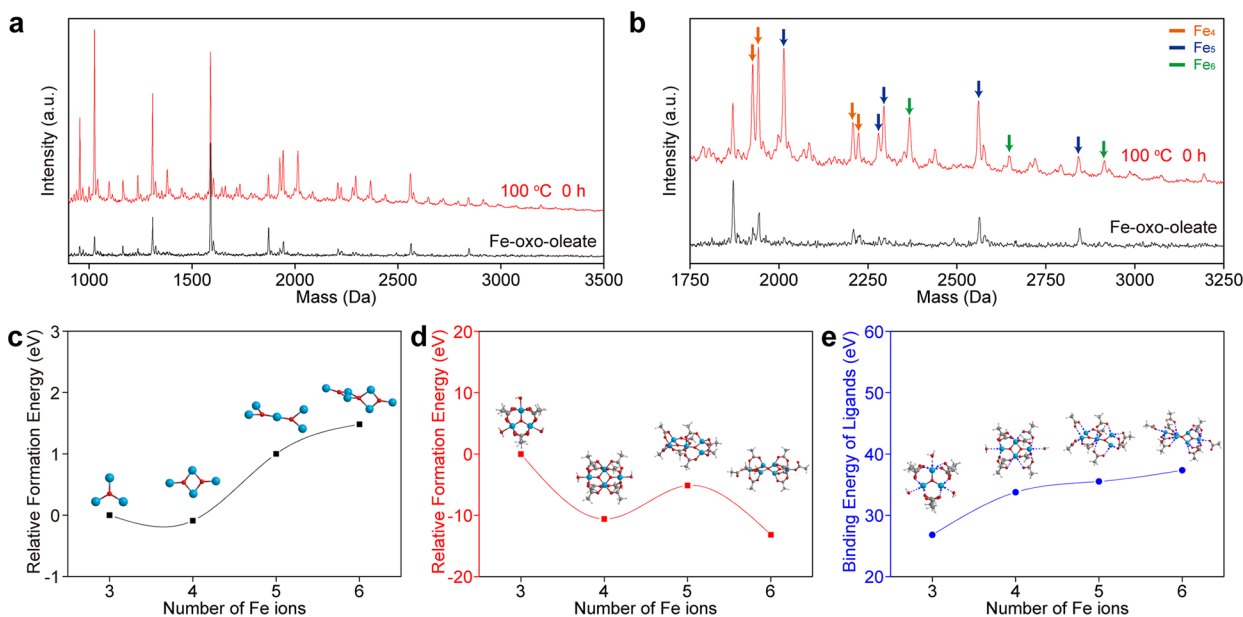


Figure 4. Change of mass spectra and relative formation energy at the early stage of esterification. (a) Mass spectra of iron-oxo-oleate (black) and *ex situ* aliquot at the early stage of esterification. (b) Detailed assignment of mass spectra: Fe₄ (orange), Fe₅ (blue), Fe₆ (green) species (see also Table S3). (c–e) Relative formation energies of the iron-oxygen core and iron-oxo clusters and binding energy of acetate ligands bound to iron-oxygen core are estimated by DFT calculation. (c) Relative formation energy of the iron-oxygen core. The formation energy of the Fe₃O core is set as 0. (d) Relative formation energy of iron-oxo clusters. The formation energy of the Fe₃O complex is set as 0. (e) Binding energy of ligands. The binding energy of ligands is calculated by subtracting the total energy with and without ligand binding moieties.

quantitatively analyzed by comparing the integration of NMR peaks for hydrogen adjacent to the ester group using hydrogen bound to the C=C double bond of the oleate group as a reference, which remains constant throughout the reaction (Figure 3a–c). The continuous increase in peak intensity of the hydrogen adjacent to the ester indicates prolonged esterification. In addition, shorter ligands are introduced to investigate the steric effect of ligands of iron-oxo clusters on the rate of esterification (Figure S9). The esterification reaction with shorter ligands (C₈) is 1.15 times faster than that with longer ligands (C₁₈), indicating that the reaction between the precursor and alcohol can be controlled by regulating the steric hindrance of ligands. The esterification reaction is important at the initial phase of the nanoparticle formation as it can result in the activation of a metal center by removing the carboxylate ligands and generating hydroxyl groups.^{23,50,51}

The reaction mechanism can be more specifically investigated by using MALDI-TOF MS, which is suitable for tracing the size distribution of nanomaterials of <5 nm (Figure 3d–f).¹¹ At the very early stage, when carboxylate ligands of iron-oxo-oleate react with the alcohol, various populations of iron-oxygen species containing different numbers of metal centers emerge in the mass spectra. Particularly, the evolution of Fe₂, Fe₄, Fe₅, and Fe₆ species is noticed after the onset of esterification (Figure 4a,b and Table S3). The formation of Fe₂, Fe₄, and Fe₅ implies that a portion of the trinuclear-oxo cluster is decomposed into smaller activated units after esterification, which can, in turn, form larger units by attaching to undecomposed trinuclear-oxo clusters. To support the suggested growth pathway, the stability of the growing iron-oxo clusters is examined by density functional theory (DFT) calculations. In DFT calculations, the metal-oxo core and carboxylate binding groups of the surface ligands are only introduced as they are the major contributors to the energy of

the iron-oxo complexes. The initial structures of different iron-oxo complexes with an increasing number of metal ions (i.e., Fe₃O, Fe₄O₂, Fe₅O₂, and Fe₆O₃) are chosen based on our MS analysis and geometrically optimized to calculate the energy of complex formation and ligand binding (Figures 4b and S10). The formation energy of iron-oxo complexes with surface ligands presents a decreasing tendency as the size of the complexes increases (Figure 4d), otherwise showing an increasing tendency without surface ligands (Figure 4c). In addition, the calculated binding energy of the carboxylate ligands on the iron-oxo core is distinctly larger than that of other types of surface ligands (Figure 4e).^{23,28–30,52,53} These results show that the strongly binding ligands reduce the formation energy of intermediate complexes, driving the pathway with a continuously increasing number of metal ions (Figure 1d).³⁹

Subsequently, through the aging process, these small iron-oxygen species gradually grow to large-sized clusters and eventually into nanoparticles typically observed in the synthesis of iron oxide nanoparticles, as presented in Figure 3e. The continuous removal of oleate ligands by esterification (Figure 3b) occurs simultaneously with continuous growth of nanoparticles from the starting tri-iron μ_3 -oxygen clusters. The iron-oxygen core can be gradually grown into larger species by condensation between hydroxyl groups of the iron-oxo clusters, which is formed after esterification of oleate ligands. Because the rate of the condensation of hydroxyl groups on the transition metal cores is fast enough,⁵⁴ the rate of continuous growth of iron oxide nanoparticles highly depends on the rate of esterification. The temperature-dependent ¹H NMR measurement shows that the rate of esterification is positively proportional to the temperature (Figure 3c). The temporal profile of the most dominant mass also reveals a pattern similar to that of the temperature-dependent rate of esterification (Figure 3f). It is noteworthy that continuous growth of

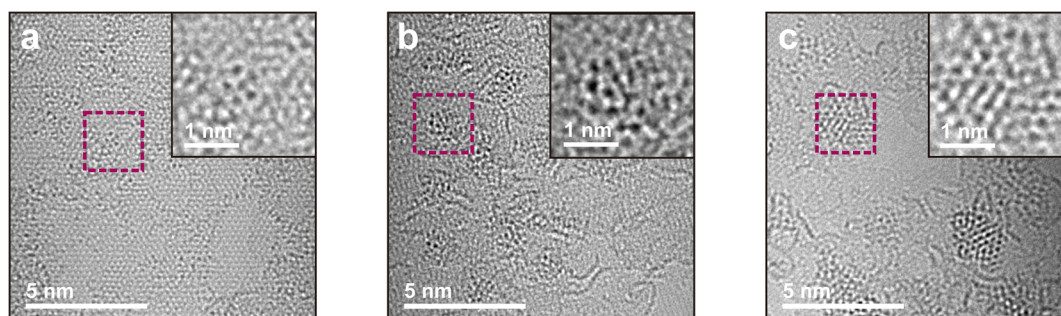


Figure 5. TEM images of iron-oxo clusters acquired from *ex situ* samples at 140 °C: (a) 0 h; (b) 4 h; and (c) 24 h aging. TEM images of iron-oxo clusters are presented in Figures S14–S16. TEM image of the bare graphene substrate is shown in Figure S17.

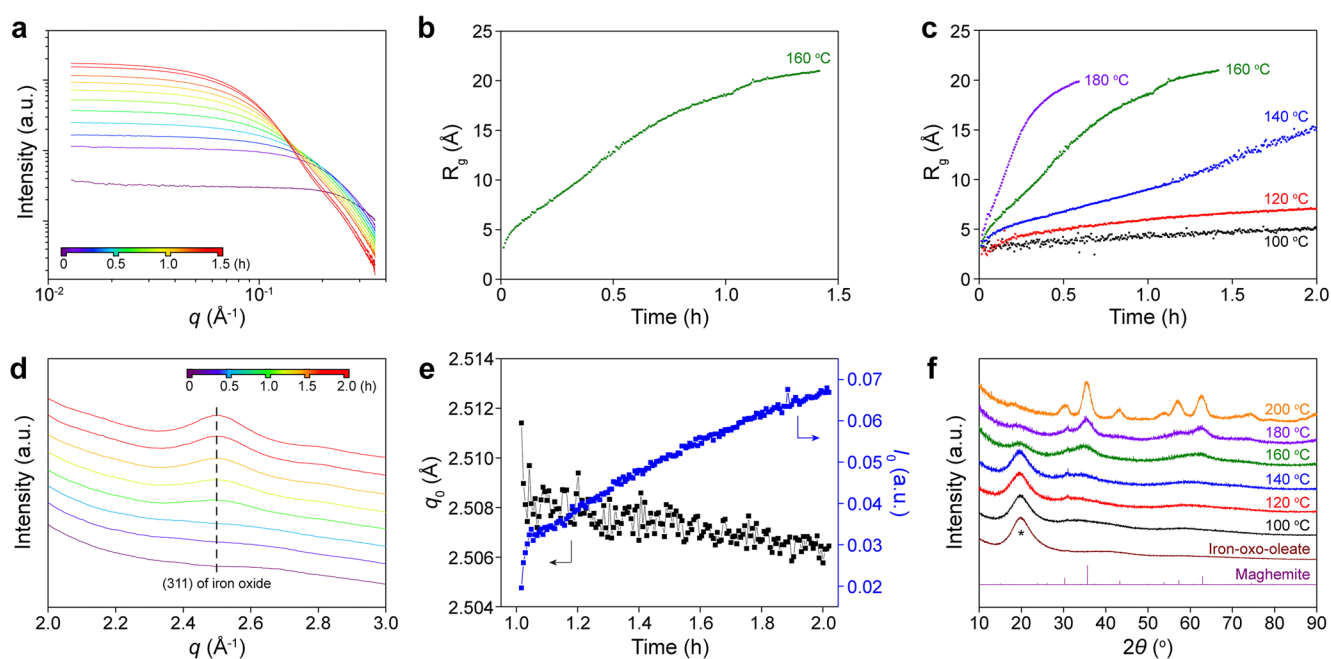


Figure 6. Confirmation of continuous growth by *in situ* X-ray scattering and X-ray diffraction. (a) Temporal evolution of small-angle X-ray scattering signals of iron-oleate precursors in 1-decanol solution. The reaction temperature is kept at 160 °C. (b) Change in radius of gyration derived from a Guinier plot from the signals in panel (a). (c) Change in radius of gyration at different aging temperatures. (d) Temporal evolution of wide-angle X-ray scattering signals of the reacting solution at 160 °C. (e) Change in peak center and intensity of scattering peaks in panel (c). (f) X-ray diffraction patterns of final products synthesized at different aging temperatures. The broad diffraction peak, marked with an asterisk, originated from disordered long-chain carboxylates.^{62,63}

nanoparticles, with the absence of distinct nucleation, is universally observed over a broad temperature range from 100 to 140 °C (Figures S11 and S12).

Continuous growth can also be examined by TEM characterization of sample aliquots taken during aging at 140 °C (Figure 5a–c). Samples for TEM analysis are prepared on graphene substrates. Because of its high electrical and thermal conductivity, the graphene substrate can minimize the electron beam effect during the TEM characterization.^{55,56} Additionally, graphene minimizes the scattering of incoming electron beams, thereby improving the contrast of small clusters.^{16,57} In the early stage of the reaction (0 h), clusters with 3–10 atoms are observed (Figures 5a and S12), and the number of atoms per cluster increases with reaction time (Figures 5b and S13). The clusters grow into small-sized nanoparticles (1.5–2.5 nm) after aging for 24 h (Figures 5c and S14). The TEM images of the iron-oxo clusters and iron oxide nanoparticles are consistent with the mass spectra, and both characterization data sets

reveal continuous growth from molecular clusters to solid oxide nanoparticles without distinct nucleation.

The continuous growth mechanism is confirmed in the ensemble level by *in situ* X-ray scattering measured at different angles. An *in situ* X-ray scattering technique has been frequently used for real-time observation of nucleation and growth processes.^{21,58–61} At a small-angle regime, iron-containing compounds are the dominant scattering species, which have a high relative scattering length density with respect to background solvent. A Guinier plot is applied to derive the radius of gyration of iron-containing species, as it can suggest dynamic changes in the ensemble of the system. A gradual increase in radius of gyration is observed, consistent with the observations from other measurements, indicating the continuous growth of iron-oxo clusters induced by esterification (Figure 6a,b). Moreover, the radius of gyrations acquired from Guinier plots shows temperature dependency, as confirmed from NMR spectroscopy and MALDI-TOF MS (Figure 6c). X-ray scattering at the wide-angle regime includes

crystallographic information on emerging iron oxide nanoparticles. The growth of clusters into nanoparticles is verified by the gradual appearance of the (311) lattice plane of iron oxide nanoparticles (Figure 6d,e). Sharp scattering peaks of the nanoparticles synthesized at high temperatures show that the crystal domain size of the product increases with increasing reaction temperature (Figure 6f).

NMR spectroscopy, mass spectrometry, electron microscopy, and X-ray scattering techniques provide consistent results supporting continuous growth from trinuclear-oxo clusters into larger iron-oxo clusters followed by the formation of iron oxide nanoparticles. Based on these characterization results, we suggest a new growth mechanism, a continuous growth model, which is induced by the controlled organic reaction between the strong binding ligands on the clusters and added alcohol in the solution. The continuous growth dominates the overall reaction process from trinuclear-oxo clusters to large-sized iron-oxo clusters and then to iron oxide nanoparticles (Figure 1). This controlled reaction pathway can be understood in the similar context of the nonhydrolytic sol-gel chemistry. At first, the controlled alcoholysis of trinuclear-oxo clusters forms hydroxyl groups on the trinuclear-oxo clusters. The trinuclear-oxo clusters containing reactive hydroxyl groups are condensed into intermediate iron-oxygen species, which have distinct numbers of iron (i.e., Fe₂, Fe₄, Fe₅, and Fe₆). These intermediate species grow into continuously profiled iron-oxo clusters from continuous supply of reactive clusters. Eventually, the nanoparticles gradually appear from the continuously growing iron-oxo clusters. This mechanism implies that the nucleation step is not distinct during the formation of the iron oxide nanoparticles studied in this report, whereas it is normally observed in the formation of many other types of nanoparticles as a prior stage to the growth regime. We believe that the absence of a distinct nucleation stage can be justified by the thermodynamic stability of the intermediate clusters regardless of their sizes due to the strong binding carboxylate groups and the controlled activation of the stabilized iron-oxo clusters.³⁹

CONCLUSION

In this work, we elucidate that the continuous growth of iron-oxo complexes into iron oxide nanoparticles is regulated by the strong binding between the metal-oxo core and carboxylate ligands. The molecular structure of iron-oleate precursors and their entire growth trajectories are extensively verified by a combination of characterization methods and theoretical calculation. As the synthetic processes for various metal-oxide nanoparticles are analogous to that we studied using metal-oleate complexes as starting precursors, the continuous growth process proposed in this work extends insights into the formation mechanism of various other metal-oxide nanoparticles.

ASSOCIATED CONTENT

Supporting Information

The Supporting Information is available free of charge on the ACS Publications website at DOI: 10.1021/jacs.9b01670.

Details of the syntheses, characterization, data processing, calculation, supporting figures and tables (PDF)

AUTHOR INFORMATION

Corresponding Authors

*myungsoo@snu.ac.kr
*jungwonpark@snu.ac.kr
*thyeon@snu.ac.kr

ORCID

Hogeun Chang: 0000-0002-3322-898X
Byung Hyo Kim: 0000-0002-4098-0053
Hu Young Jeong: 0000-0002-5550-5298
Kwangsoo Shin: 0000-0001-5337-0679
Jiwoong Yang: 0000-0002-2346-8197
Hoonkyung Lee: 0000-0002-6417-1648
Jungwon Park: 0000-0003-2927-4331
Taeghwan Hyeon: 0000-0001-5959-6257

Author Contributions

▽H.C. and B.H.K. contributed equally to this work.

Notes

The authors declare no competing financial interest.

ACKNOWLEDGMENTS

This work was supported by the Research Center Program of Institute for Basic Science, Korea (IBS-R006-D1). Experiments at PAL-II 9A U-SAXS beamline were supported in part by MEST and POSTECH. H.Y.J. acknowledges the support from Creative Materials Discovery Program through the National Research Foundation of Korea (NRF-2016M3D1A1900035). J.P. acknowledges support from the National Research Foundation of Korea (NRF) grant funded by the Korea Government (MSIT) (NRF-2017R1A5A1015365 and NRF-2017R1C1B2010434). Also, we especially thank Dr. Hyungju Ahn of Pohang Accelerator Laboratory for helpful discussion on X-ray scattering, and Kyung Hee Lim of the National Center for Inter-University Research Facilities (NCIRF) for cross-checking MALDI-TOF MS experiments.

REFERENCES

- (1) LaMer, V. K.; Dinegar, R. H. Theory, production and mechanism of formation of monodispersed hydrosols. *J. Am. Chem. Soc.* **1950**, *72*, 4847–4854.
- (2) Talapin, D. V.; Rogach, A. L.; Haase, M.; Weller, H. Evolution of an ensemble of nanoparticles in a colloidal solution: theoretical study. *J. Phys. Chem. B* **2001**, *105*, 12278–12285.
- (3) Kwon, S. G.; Hyeon, T. Formation mechanisms of uniform nanocrystals via hot-injection and heat-up methods. *Small* **2011**, *7*, 2685–2702.
- (4) Murray, C. B.; Norris, D. J.; Bawendi, M. G. Synthesis and characterization of nearly monodisperse CdE (E = sulfur, selenium, tellurium) semiconductor nanocrystallites. *J. Am. Chem. Soc.* **1993**, *115*, 8706–8715.
- (5) Kwon, S. G.; Piao, Y.; Park, J.; Angappane, S.; Jo, Y.; Hwang, N. M.; Park, J. G.; Hyeon, T. Kinetics of monodisperse iron oxide nanocrystal formation by "heating-up" process. *J. Am. Chem. Soc.* **2007**, *129*, 12571–12584.
- (6) Owen, J. S.; Chan, E. M.; Liu, H.; Alivisatos, A. P. Precursor conversion kinetics and the nucleation of cadmium selenide nanocrystals. *J. Am. Chem. Soc.* **2010**, *132*, 18206–18213.
- (7) Evans, C. M.; Evans, M. E.; Krauss, T. D. Mysteries of TOPSe revealed: insights into quantum dot nucleation. *J. Am. Chem. Soc.* **2010**, *132*, 10973–10975.
- (8) Goulet, P. J.; Lennox, R. B. New insights into Brust-Schiffrin metal nanoparticle synthesis. *J. Am. Chem. Soc.* **2010**, *132*, 9582–9584.

- (9) Cossairt, B. M.; Owen, J. S. CdSe clusters: at the interface of small molecules and quantum dots. *Chem. Mater.* **2011**, *23*, 3114–3119.
- (10) Watzky, M. A.; Finke, R. G. Transition metal nanocluster formation kinetic and mechanistic studies. A new mechanism when hydrogen is the reductant: slow, continuous nucleation and fast autocatalytic surface growth. *J. Am. Chem. Soc.* **1997**, *119*, 10382–10400.
- (11) Kim, B. H.; Shin, K.; Kwon, S. G.; Jang, Y.; Lee, H. S.; Lee, H.; Jun, S. W.; Lee, J.; Han, S. Y.; Yim, Y. H.; Kim, D. H.; Hyeon, T. Sizing by weighing: characterizing sizes of ultrasmall-sized iron oxide nanocrystals using MALDI-TOF mass spectrometry. *J. Am. Chem. Soc.* **2013**, *135*, 2407–2410.
- (12) Wang, F.; Richards, V. N.; Shields, S. P.; Buhro, W. E. Kinetics and mechanisms of aggregative nanocrystal growth. *Chem. Mater.* **2014**, *26*, 5–21.
- (13) Lee, J.; Yang, J.; Kwon, S. G.; Hyeon, T. Nonclassical nucleation and growth of inorganic nanoparticles. *Nat. Rev. Mater.* **2016**, *1*, 16034.
- (14) Liu, M.; Wang, K.; Wang, L.; Han, S.; Fan, H.; Rowell, N.; Ripmeester, J. A.; Renoud, R.; Bian, F.; Zeng, J.; Yu, K. Probing intermediates of the induction period prior to nucleation and growth of semiconductor quantum dots. *Nat. Commun.* **2017**, *8*, 15467.
- (15) Zheng, H.; Smith, R. K.; Jun, Y.-w.; Kisielowski, C.; Dahmen, U.; Alivisatos, A. P. Observation of single colloidal platinum nanocrystal growth trajectories. *Science* **2009**, *324*, 1309–1312.
- (16) Yuk, J. M.; Park, J.; Ercius, P.; Kim, K.; Hellebusch, D. J.; Crommie, M. F.; Lee, J. Y.; Zettl, A.; Alivisatos, A. P. High-resolution EM of colloidal nanocrystal growth using graphene liquid cells. *Science* **2012**, *336*, 61–64.
- (17) Loh, N. D.; Sen, S.; Bosman, M.; Tan, S. F.; Zhong, J.; Nijhuis, C. A.; Kral, P.; Matsudaira, P.; Mirsaidov, U. Multistep nucleation of nanocrystals in aqueous solution. *Nat. Chem.* **2017**, *9*, 77–82.
- (18) Wu, Z.; Yang, S.; Wu, W. Shape control of inorganic nanoparticles from solution. *Nanoscale* **2016**, *8*, 1237–1259.
- (19) Chan, E. M.; Xu, C.; Mao, A. W.; Han, G.; Owen, J. S.; Cohen, B. E.; Milliron, D. J. Reproducible, high-throughput synthesis of colloidal nanocrystals for optimization in multidimensional parameter space. *Nano Lett.* **2010**, *10*, 1874–1885.
- (20) Kang, Y.; Li, M.; Cai, Y.; Cargnello, M.; Diaz, R. E.; Gordon, T. R.; Wieder, N. L.; Adzic, R. R.; Gorte, R. J.; Stach, E. A.; Murray, C. B. Heterogeneous catalysts need not be so "heterogeneous": monodisperse Pt nanocrystals by combining shape-controlled synthesis and purification by colloidal recrystallization. *J. Am. Chem. Soc.* **2013**, *135*, 2741–2747.
- (21) Kwon, S. G.; Krylova, G.; Phillips, P. J.; Klie, R. F.; Chattopadhyay, S.; Shibata, T.; Bunel, E. E.; Liu, Y.; Prakapenka, V. B.; Lee, B.; Shevchenko, E. V. Heterogeneous nucleation and shape transformation of multicomponent metallic nanostructures. *Nat. Mater.* **2015**, *14*, 215–223.
- (22) Hendricks, M. P.; Campos, M. P.; Cleveland, G. T.; Jen-La Plante, I.; Owen, J. S. A tunable library of substituted thiourea precursors to metal sulfide nanocrystals. *Science* **2015**, *348*, 1226–1230.
- (23) De Roo, J.; Van Driessche, I.; Martins, J. C.; Hens, Z. Colloidal metal oxide nanocrystal catalysis by sustained chemically driven ligand displacement. *Nat. Mater.* **2016**, *15*, 517–521.
- (24) Xie, L.; Shen, Y.; Franke, D.; Sebastian, V.; Bawendi, M. G.; Jensen, K. F. Characterization of Indium Phosphide Quantum Dot Growth Intermediates Using MALDI-TOF Mass Spectrometry. *J. Am. Chem. Soc.* **2016**, *138*, 13469–13472.
- (25) Gary, D. C.; Flowers, S. E.; Kaminsky, W.; Petrone, A.; Li, X.; Cossairt, B. M. Single-Crystal and Electronic Structure of a 1.3 nm Indium Phosphide Nanocluster. *J. Am. Chem. Soc.* **2016**, *138*, 1510–1513.
- (26) Frenette, L. C.; Krauss, T. D. Uncovering active precursors in colloidal quantum dot synthesis. *Nat. Commun.* **2017**, *8*, 2082.
- (27) Guntlin, C. P.; Ochsenbein, S. T.; Wörle, M.; Erni, R.; Kravchyk, K. V.; Kovalenko, M. V. Popcorn-shaped Fe_xO (wüstite) nanoparticles from a single-source precursor: colloidal synthesis and magnetic properties. *Chem. Mater.* **2018**, *30*, 1249–1256.
- (28) Puzder, A.; Williamson, A. J.; Zaitseva, N.; Galli, G.; Manna, L.; Alivisatos, A. P. The effect of organic ligand binding on the growth of CdSe nanoparticles probed by *ab initio* calculations. *Nano Lett.* **2004**, *4*, 2361–2365.
- (29) Manna, L.; Wang, L. W.; Cingolani, R.; Alivisatos, A. P. First-principles modeling of unpassivated and surfactant-passivated bulk facets of wurtzite CdSe: a model system for studying the anisotropic growth of CdSe nanocrystals. *J. Phys. Chem. B* **2005**, *109*, 6183–6192.
- (30) Rempel, J. Y.; Trout, B. L.; Bawendi, M. G.; Jensen, K. F. Density functional theory study of ligand binding on CdSe (0001), (0001), and (1120) single crystal relaxed and reconstructed surfaces: implications for nanocrystalline growth. *J. Phys. Chem. B* **2006**, *110*, 18007–18016.
- (31) van Embden, J.; Mulvaney, P. Nucleation and growth of CdSe nanocrystals in a binary ligand system. *Langmuir* **2005**, *21*, 10226–10233.
- (32) Joo, J.; Son, J. S.; Kwon, S. G.; Yu, J. H.; Hyeon, T. Low-temperature solution-phase synthesis of quantum well structured CdSe nanoribbons. *J. Am. Chem. Soc.* **2006**, *128*, 5632–5633.
- (33) Yu, J. H.; Liu, X.; Kweon, K. E.; Joo, J.; Park, J.; Ko, K. T.; Lee, D. W.; Shen, S.; Tivakornsasithorn, K.; Son, J. S.; Park, J. H.; Kim, Y. W.; Hwang, G. S.; Dobrowolska, M.; Furdyna, J. K.; Hyeon, T. Giant Zeeman splitting in nucleation-controlled doped CdSe:Mn²⁺ quantum nanoribbons. *Nat. Mater.* **2010**, *9*, 47–53.
- (34) Yang, J.; Fainblat, R.; Kwon, S. G.; Muckel, F.; Yu, J. H.; Terlinden, H.; Kim, B. H.; Iavarone, D.; Choi, M. K.; Kim, I. Y.; Park, I.; Hong, H. K.; Lee, J.; Son, J. S.; Lee, Z.; Kang, K.; Hwang, S. J.; Bacher, G.; Hyeon, T. Route to the Smallest Doped Semiconductor: Mn²⁺-Doped (CdSe)₁₃ Clusters. *J. Am. Chem. Soc.* **2015**, *137*, 12776–12779.
- (35) Pearson, R. G. Hard and Soft Acids and Bases. *J. Am. Chem. Soc.* **1963**, *85*, 3533–3539.
- (36) Joo, J.; Kwon, S. G.; Yu, J. H.; Hyeon, T. Synthesis of ZnO Nanocrystals with Cone, Hexagonal Cone, and Rod Shapes via Non-Hydrolytic Ester Elimination Sol–Gel Reactions. *Adv. Mater.* **2005**, *17*, 1873–1877.
- (37) Niederberger, M. Nonaqueous sol-gel routes to metal oxide nanoparticles. *Acc. Chem. Res.* **2007**, *40*, 793–800.
- (38) Kwon, S. G.; Hyeon, T. Colloidal chemical synthesis and formation kinetics of uniformly sized nanocrystals of metals, oxides, and chalcogenides. *Acc. Chem. Res.* **2008**, *41*, 1696–1709.
- (39) Gatteschi, D.; Caneschi, A.; Sessoli, R.; Cornia, A. Magnetism of large iron-oxo clusters. *Chem. Soc. Rev.* **1996**, *25*, 101–109.
- (40) Park, J.; An, K.; Hwang, Y.; Park, J. G.; Noh, H. J.; Kim, J. Y.; Park, J. H.; Hwang, N. M.; Hyeon, T. Ultra-large-scale syntheses of monodisperse nanocrystals. *Nat. Mater.* **2004**, *3*, 891–895.
- (41) (a) Mehrotra, R. C.; Bohra, R. *Metal Carboxylates*; Academic Press, 1983. (b) McCleverty, J. A.; Meyer, T. J. *Comprehensive Coordination Chemistry II*; Elsevier Ltd., 2004; Vol. 5.
- (42) Oh, S. M.; Hendrickson, D. N.; Hassett, K. L.; Davis, R. E. Electron transfer in mixed-valence, oxo-centered, trinuclear iron acetate complexes: effect of statically disordered to dynamically disordered transformation in the solid state. *J. Am. Chem. Soc.* **1984**, *106*, 7984–7985.
- (43) Oh, S. M.; Hendrickson, D. N.; Hassett, K. L.; Davis, R. E. Valence-detraping modes for electron transfer in the solid state of mixed-valence, oxo-centered, trinuclear iron acetate complexes: x-ray structure and physical data for [Fe₃O(O₂CCH₃)₆(4-Et-py)₃](4-Et-py). *J. Am. Chem. Soc.* **1985**, *107*, 8009–8018.
- (44) Long, G. J.; Robinson, W. T.; Tappmeyer, W. P.; Bridges, D. L. The magnetic, electronic, and Mössbauer spectral properties of several trinuclear iron(III) carboxylate complexes. *J. Chem. Soc., Dalton Trans.* **1973**, 573–579.
- (45) Blake, A. B.; Yavari, A.; Hatfield, W. E.; Sethulekshmi, C. N. Magnetic and spectroscopic properties of some heterotrinuclear basic acetates of chromium(III), iron(III), and divalent metal ions. *J. Chem. Soc., Dalton Trans.* **1985**, 2509–2520.

- (46) Abrahamson, H. B.; Lukaski, H. C. Synthesis and characterization of iron stearate compounds. *J. Inorg. Biochem.* **1994**, *54*, 115–130.
- (47) Baran, P.; Boča, R.; Chakraborty, I.; Giapintzakis, J.; Herchel, R.; Huang, Q.; McGrady, J. E.; Raptis, R. G.; Sanakis, Y.; Simopoulos, A. Synthesis, Characterization, and Study of Octanuclear Iron-Oxo Clusters Containing a Redox-Active Fe₄O₄-Cubane Core. *Inorg. Chem.* **2008**, *47*, 645–655.
- (48) Nakamoto, K. *Infrared and Raman Spectra of Inorganic and Coordination Compounds*; John Wiley & Sons, Inc.: Hoboken, NJ, 2008.
- (49) Lynch, J.; Zhuang, J.; Wang, T.; LaMontagne, D.; Wu, H.; Cao, Y. C. Gas-bubble effects on the formation of colloidal iron oxide nanocrystals. *J. Am. Chem. Soc.* **2011**, *133*, 12664–12674.
- (50) Kim, B. H.; Lee, N.; Kim, H.; An, K.; Park, Y. I.; Choi, Y.; Shin, K.; Lee, Y.; Kwon, S. G.; Na, H. B.; Park, J. G.; Ahn, T. Y.; Kim, Y. W.; Moon, W. K.; Choi, S. H.; Hyeon, T. Large-scale synthesis of uniform and extremely small-sized iron oxide nanoparticles for high-resolution T¹ magnetic resonance imaging contrast agents. *J. Am. Chem. Soc.* **2011**, *133*, 12624–12631.
- (51) Ito, D.; Yokoyama, S.; Zaikova, T.; Masuko, K.; Hutchison, J. E. Synthesis of ligand-stabilized metal oxide nanocrystals and epitaxial core/shell nanocrystals via a lower-temperature esterification process. *ACS Nano* **2014**, *8*, 64–75.
- (52) Harris, R. A.; Shumbula, P. M.; van der Walt, H. Analysis of the interaction of surfactants oleic acid and oleylamine with iron oxide nanoparticles through molecular mechanics modeling. *Langmuir* **2015**, *31*, 3934–3943.
- (53) Al-Johani, H.; Abou-Hamad, E.; Jedidi, A.; Widdifield, C. M.; Viger-Gravel, J.; Sangaru, S. S.; Gajan, D.; Anjum, D. H.; Ould-Chikh, S.; Hedhili, M. N.; Gurinov, A.; Kelly, M. J.; El Eter, M.; Cavallo, L.; Emsley, L.; Basset, J. M. The structure and binding mode of citrate in the stabilization of gold nanoparticles. *Nat. Chem.* **2017**, *9*, 890–895.
- (54) Jao, M.-H.; Cheng, C.-C.; Lu, C.-F.; Hsiao, K.-C.; Su, W.-F. Low temperature and rapid formation of high quality metal oxide thin film via a hydroxide-assisted energy conservation strategy. *J. Mater. Chem. C* **2018**, *6*, 9941–9949.
- (55) Nair, R. R.; Blake, P.; Blake, J. R.; Zan, R.; Anissimova, S.; Bangert, U.; Golovanov, A. P.; Morozov, S. V.; Geim, A. K.; Novoselov, K. S.; Latychevskaia, T. Graphene as a transparent conductive support for studying biological molecules by transmission electron microscopy. *Appl. Phys. Lett.* **2010**, *97*, 153102.
- (56) Bosch-Navarro, C.; Laker, Z. P.; Thomas, H. R.; Marsden, A. J.; Sloan, J.; Wilson, N. R.; Rourke, J. P. Covalently binding atomically designed Au₉ clusters to chemically modified graphene. *Angew. Chem., Int. Ed.* **2015**, *54*, 9560–9563.
- (57) Park, J.; Elmlund, H.; Ercius, P.; Yuk, J. M.; Limmer, D. T.; Chen, Q.; Kim, K.; Han, S. H.; Weitz, D. A.; Zettl, A.; Alivisatos, A. P. 3D structure of individual nanocrystals in solution by electron microscopy. *Science* **2015**, *349*, 290–295.
- (58) Polte, J.; Ahner, T. T.; Delissen, F.; Sokolov, S.; Emmerling, F.; Thunemann, A. F.; Kraehnert, R. Mechanism of gold nanoparticle formation in the classical citrate synthesis method derived from coupled *in situ* XANES and SAXS evaluation. *J. Am. Chem. Soc.* **2010**, *132*, 1296–1301.
- (59) Abecassis, B.; Bouet, C.; Garnero, C.; Constantin, D.; Lequeux, N.; Ithurria, S.; Dubertret, B.; Pauw, B. R.; Pontoni, D. Real-time *in situ* probing of high-temperature quantum dots solution synthesis. *Nano Lett.* **2015**, *15*, 2620–2626.
- (60) Lassenberger, A.; Grunewald, T. A.; van Oostrum, P. D. J.; Rennhofer, H.; Amenitsch, H.; Zirbs, R.; Lichtenegger, H. C.; Reimhult, E. Monodisperse iron oxide nanoparticles by thermal decomposition: elucidating particle formation by second-resolved *in situ* small-angle X-ray scattering. *Chem. Mater.* **2017**, *29*, 4511–4522.
- (61) Maes, J.; Castro, N.; De Nolf, K.; Walravens, W.; Abecassis, B.; Hens, Z. Size and Concentration Determination of Colloidal Nanocrystals by Small-Angle X-ray Scattering. *Chem. Mater.* **2018**, *30*, 3952–3962.
- (62) Jandacek, R. J.; Broering, W. B. X-ray diffraction study of sodium soaps of monounsaturated and polyunsaturated fatty acids. *Lipids* **1989**, *24*, 1008–1013.
- (63) Corkery, R. W. A variation on Luzzati's soap phases. Room temperature thermotropic liquid crystals. *Phys. Chem. Chem. Phys.* **2004**, *6*, 1534–1546.